

Wake effects of large offshore wind farms identified from satellite SAR

Merete Bruun Christiansen*, Charlotte B. Hasager

Risø National Laboratory, Roskilde, Denmark

Received 18 March 2005; received in revised form 21 July 2005; accepted 22 July 2005

Abstract

The effect of large offshore wind farms on the local wind climate is studied using satellite synthetic aperture radar (SAR). Wind maps are derived from a total of 30 ERS-2 SAR scenes and 11 Envisat ASAR scenes over two large offshore wind farms in Denmark: Horns Rev in the North Sea (80 turbines) and Nysted in the Baltic Sea (78 turbines). The wind farms are the world's largest to date. **For the first time, high-resolution SAR-derived wind speed images are utilized to identify regions of reduced wind speed and high turbulence intensity** (i.e. wind wakes) downstream of wind turbine arrays. After quality control, 19 SAR scenes are available for the study of wake effects. A decrease of the mean wind speed is found as the wind flows through the wind farms, leaving a velocity deficit of 8–9% on average, immediately downstream of the wind turbine arrays. From this point, wind speed recovers to within 2% of the free stream velocity over a distance of 5–20 km depending on the ambient wind speed, the atmospheric stability and the number of turbines in operation. **The wake magnitude and extent found from SAR wind maps is consistent with in situ measurements and results from wake models.** The standard deviation of SAR-derived wind speeds is an indicator of turbulence intensity. Added turbulence intensity downstream of a wind farm is found for 7 of the 19 cases. Turbulence intensity is not as easily identified from SAR images as changes in the mean wind speed. This may be due to a low impact of wind turbine generated turbulence on the sea surface where SAR measurements are obtained.

© 2005 Elsevier Inc. All rights reserved.

Keywords: Synthetic aperture radar; ERS-2; ENVISAT; Wind energy; Wind turbines; Wake effects

1. Introduction

The wind provides a rich energy resource which, together with other renewable energy resources, must be exploited further to meet the major energy challenges in the world today. Industrialization is causing a demand for energy that fossil fuel supplies are insufficient to meet in the long term (WEC, 2001). Following debates on global warming, many nations have set targets to stabilize levels of greenhouse gas emission from the burning of fossil fuel (WEC, 2000). There is a call for a sustainable and clean energy supply (WEC, 2003). The worldwide capacity of wind energy is rapidly growing. In 2003, installed capacity grew to approximately 40 GW (IEA, 2004). The prospect of

installing wind power offshore has led to optimistic views upon the potential of wind energy, especially in Europe where 10 GW of offshore capacity is expected to be installed by 2010 (EWEA, 2004). The offshore capacity installed by the end of 2003 was 0.6 GW (IEA, 2004). Offshore wind farms are operating in Denmark, Germany, Ireland, the Netherlands, Sweden and the United Kingdom; several other nations have specific offshore plans.

Some concern has been expressed about the impact of large scale use of wind power on the local and global meteorology (Keith et al., 2004; Roy et al., 2004). Attempts to balance the positive and negative environmental impacts of wind power are relevant for energy planning (Christiansen, 2004). Building an offshore wind farm requires a large capital investment, thus it is crucial to identify sites with optimum predicted power outputs. As the most ideal sites become occupied, there is a growing interest in constructing multiple wind farms within the same area, which also allows a sharing of grid connections. Wind shadowing between

* Corresponding author. Tel.: +45 4677 5002; fax: +45 4677 5970.

E-mail address: merete.bruun.christiansen@risoe.dk
(M.B. Christiansen).

wind farm arrays should be minimized. It is thus necessary to quantify the magnitude and extent of wind wakes (i.e. regions of reduced wind speed and increased turbulence intensity) downstream of wind farms.

The opportunity to determine ocean wind fields from satellite images is highly attractive in offshore wind energy studies because satellite images provide spatial information that cannot be gathered from traditional meteorological measurements. The objective of the present study is to use synthetic aperture radar (SAR) measurements from the ERS-2 and Envisat satellite missions to derive wind fields over the ocean and to utilize this satellite information to identify wind wakes downstream of two large offshore wind farms in Denmark. Wind speed has previously been derived successfully from SAR; a review is provided by Monaldo and Kerbaol (2003). Chunchuzov et al. (2000) have detected wakes on the lee side of an offshore platform from ERS-2 and RADARSAT SAR data and Li et al. (2000) have characterized atmospheric vortex streets from a RADARSAT image. Other examples of SAR scenes showing the wake phenomena downstream of islands and mountains are given by Young and Winstead (2004). We expect that wakes of large offshore wind farms can also be detected from satellite SAR measurements. Hypothetically, the magnitude and spatial extent of such wind wakes depend on the ambient wind speed, the atmospheric stability, and up to a certain threshold, the number of wind turbines in operation. Rotating turbine blades generate turbulence with characteristic length scales around 0.5 km (Petersen et al., 1998). If the turbulence persists at the sea surface, we can expect to detect it from the standard deviation in SAR wind speed measurements provided that the spatial resolution is sufficient.

The paper is structured as follows: Sections 2–4 provide background information on SAR; derivation of wind fields from SAR; wind turbines and wake effects. In Section 5 is a description of the site and data used and in Section 6, the data processing methods are described. Results are presented in Section 7, leading to discussion and conclusion in Sections 8 and 9, respectively.

2. Synthetic Aperture Radar (SAR)

SAR instruments are side-looking active microwave sensors mounted on a satellite or aircraft and typically operating at centimetre to decimetre scale wavelengths. The radar signal penetrates clouds and light rain and is independent of sunlight, hence SAR systems operate day and night. Emitted radar pulses interact with surface roughness elements whose size is comparable to the radar wavelength. Bragg scattering is dominant, but specular reflection contributes to the return signal when surface facets oriented perpendicular to the radar beam are illuminated. The radar signal scattered from the Earth surface back to the sensor is the backscatter coefficient, σ^0 . A SAR measures time delay and Doppler frequency to

produce high-resolution images where the image value is proportional to σ^0 (Ulaby et al., 1982).

Numerous system and target parameters affect σ^0 (Lewis & Henderson, 1998): surface roughness relative to the system wavelength determines the extent of radar cross section associated with Bragg scattering. The local incidence angle, which is a combination of the radar incidence angle and the terrain slope is important, too. Large angles (far range) are associated with low σ^0 values, while σ^0 increases at small angles (near range). Asymmetric objects (e.g. surface waves) appear differently in SAR images depending on the radar look direction relative to the object orientation. Over the ocean, maximum radar return occurs for waves travelling towards the radar. Geometrical errors are introduced as the radar scans tall objects on the Earth surface (e.g. wind turbines): radar shadowing occurs if the area behind an obstacle is not illuminated. Positioning of tall objects within a SAR image is biased if the object top is illuminated before the base. The different time delays associated with returns from the top and bottom of the object may cause misplacement of image intensity in the projected ground range image. This effect is called layover. Moving targets (e.g. wind turbine rotor blades) affect the Doppler frequency measured by the SAR if the turbine motion is along the radar line of sight.

The ERS-2 satellite has a 35-day repeat track and a re-visit period of approximately 10 days at mid-latitudes. The ERS-2 SAR operates at C-band (5.3 GHz) and at vertical receive and transmit polarization (VV). The SAR scans the Earth surface at incidence angles of 20–26° in a 100 km wide swath. Each scene covers an area of 100 by 100 km with a nominal spatial resolution of 25 m in range and 6 m in azimuth. During pre-processing, multi-looking is used to reduce speckle noise (i.e. random noise found in all SAR images). Typically, users receive three-look precision (PRI) images with a range and azimuth spatial resolution of 25 m (Attema et al., 2000).

The Envisat orbit and re-visit period are similar to those of ERS-2. Envisat carries a C-band Advanced Synthetic Aperture Radar (ASAR). This instrument is capable of scanning in several different modes over a wide range of incidence angles, resulting in many different product types. For the present study, scenes in Image Mode (IMP) and Alternating Polarization Mode (APP) are used. Images in IMP mode have four looks whereas images in APP mode have two looks. The products have coverage and spatial resolution comparable to ERS-2 PRI products and both HH and VV polarization are available. Only VV polarization is used here as the backscatter-to-wind relationship is better understood than for HH polarization.

3. Derivation of ocean wind fields from SAR

In offshore areas, C-band SAR signals interact with gravity-capillary waves. These centimeter-scale waves

respond instantaneously (within less than one second) to the strength of the local wind. Since wave crests tend to align perpendicular to the local wind direction, σ^0 is wind direction dependent.

In order to derive wind fields from SAR, either wind speed or direction must be known a priori. For wind energy studies, wind speed is usually desired, therefore the wind direction is used as input. Information on wind direction may be obtained with a 180° ambiguity from wind streaks that are often seen on SAR images as linear features aligned approximately with the wind direction. The streaks are generated by atmospheric roll vortices (Gerling, 1986; Mourad et al., 2000). Methods to identify streak directions are: FFT (Lehner et al., 1998; Vachon & Dobson, 1996), wavelet analysis (Du et al., 2002; Fichaux & Rachin, 2002), and the local gradient method (Horstmann & Koch, 2003; Koch, 2004). Wind directions may be estimated from atmospheric models (Monaldo, 2000; Monaldo et al., 2001), scatterometer measurements (Monaldo et al., 2004) or, if available, offshore meteorological measurements (Hasager et al., 2004b). Meteorological measurements are suitable in areas where a limited spatial variability of the wind direction is expected.

The backscatter coefficient is related to wind speed and direction through geophysical model functions such as CMOD-4, originally developed for scatterometer winds (Stoffelen & Anderson, 1997a,b). The simple, general form of this empirical algorithm is:

$$\sigma^0 = U^\gamma (a_0 + a_1 \cos \phi + a_2 \cos 2\phi) \quad (1)$$

where σ^0 is the backscatter coefficient, U is wind speed (m s^{-1}) and ϕ is wind direction relative to the radar look direction. σ^0 is a function of incidence angle and wind speed contained in the parameters a_0 , a_1 , a_2 and γ . The model function is valid for wind speeds at 10 m above the surface for a neutral stability atmosphere, having a logarithmic profile of wind speed with height. Generally, wind speeds in the range of 2–24 m s^{-1} can be mapped with an accuracy of $\pm 2 \text{ m s}^{-1}$ for incidence angles of 20–60° (Stoffelen & Anderson, 1993). RMS errors as low as $\pm 1.3 \text{ m s}^{-1}$ have been reported for SAR wind speed estimates (Hasager et al., 2004b). Since geophysical model functions are derived from open water conditions, bias is expected as they are applied to fetch-limited seas where the surface roughness is influenced by a number of parameters other than the wind stress. For example, changes in atmospheric stability can change the relationship between wind speed and σ^0 . Oceanic noise is caused by bathymetry, tidal currents, oceanic internal waves, sea ice, and surfactants (Clemente-Colón & Yan, 2000). In order to reduce contamination due to non-atmospheric processes, it is recommended to average pixels in ERS-2 SAR and Envisat ASAR images to 400–500 m although spatial detail is lost through such a decrease in resolution (Horstmann et al., 2000; Mourad et al., 2000; Hasager et al., 2004b).

4. Wind turbines and wake effects

Installation of wind power offshore is more acceptable to local communities than land based installations because noise and visual disturbance is limited. Moving offshore allows large arrays of wind turbines to be installed on high towers. Power outputs are generally higher offshore than on land because turbines are operating at higher levels above the surface. Also, higher wind speed and lower turbulence intensity are found offshore. Currently, wind turbines must be installed in shallow waters (i.e. water depths up to 20 m). Offshore wind farms are therefore located relatively close to shore where flow conditions are affected by land. For offshore winds, an increase of wind speed and a reduction of turbulence is typically found with increasing distance from land. However, effects of land on the near-shore wind climate and the distance over which they propagate are still poorly understood (Barthelmie & Pryor, in press).

Wind turbines start operating as the mean wind speed exceeds a threshold known as the *cut-in* wind speed. The cut-in wind speed ranges 3–5 m s^{-1} depending on turbine manufacturer. Once the turbines are running, power output increases with wind speed up to approximately 15 m s^{-1} , which is the *nominal* wind speed. Above the nominal wind speed, power production is fixed regardless of wind speed up to the *cut-out* wind speed of 25 m s^{-1} , where the turbines are shut down for safety reasons.

As the wind approaches the rotor plane of a single wind turbine, pressure increases and air is deflected around the rotor plane. This fraction of the wind is never used to drive the turbine. Kinetic energy is extracted from the fraction of wind passing through the turbine rotor plane. A maximum of 16/27 (59%) of the kinetic energy of the wind can be converted to power (Betz, 1920). Energy extraction slows down the wind and the wind speed measured just downstream of a turbine is significantly lower than the free stream velocity. Near hub-height, the air is also more turbulent. The downstream region, over which the wind climate is affected by a wind turbine, is called a wind wake; it is characterized by the relative velocity deficit, VD in percent:

$$\text{VD} = \frac{U_{\text{freestream}} - U_{\text{wake}}}{U_{\text{freestream}}} 100\% \quad (2)$$

where $U_{\text{freestream}}$ is the non-obstructed mean wind speed. $U_{\text{freestream}}$ is typically observed upstream of a wind farm and U_{wake} is observed in the wake. Both $U_{\text{freestream}}$ and U_{wake} are generally derived from meteorological time-series observations at fixed points in space. Wind wakes are also characterized by turbulence intensity, I in percent:

$$I = \frac{\sigma_U}{U} 100\% \quad (3)$$

where U is the mean wind speed and σ_U is wind speed standard deviation.

Assuming no compression, the amount of air leaving the turbine rotor plane equals the amount entering. Fig. 1

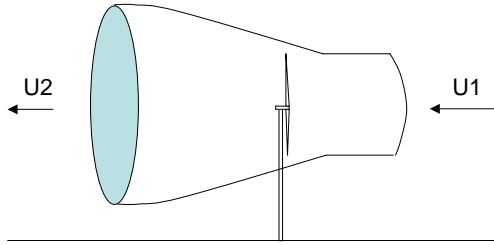


Fig. 1. Cone shaped wake downstream of a single wind turbine. U_1 and U_2 are upstream and downstream wind speeds, respectively.

illustrates how this principle leads to a cone shaped wake. The wake radius increases with the downstream distance and when the radius exceeds the turbine hub-height, the wake impacts the surface. This occurs at a downstream distance equivalent to 10 rotor diameters (Frandsen et al., 2004). Beyond this distance, wake effects should, in principle, be detectable by satellite SAR systems.

A large gradient of wind speed is found near the boundary between a wake and the ambient air surrounding it, but at some distance downstream from the wind turbine, turbulent diffusion causes the wake to diminish. Since diffusion is inhibited in stable atmospheres and enhanced in unstable, the persistence of wind wakes, in time and space, depends on atmospheric stability. Maximum wake effects are expected at wind speeds of $8\text{--}10\text{ m s}^{-1}$ (Frandsen & Hauge Madsen, 2003). As the wind speed exceeds the nominal wind speed, a smaller fraction of kinetic energy is

taken out of the flow, thus the velocity deficit is reduced. Turning of wind wakes due to the Coriolis force is very small and usually neglected in wake studies. However, wake meandering may occur (Crespo et al., 1999).

Wake effects are not easily identified through traditional meteorological measurements, because wakes are spatial phenomena shifting with the direction of the wind. Erection and maintenance of meteorological towers offshore is costly; therefore measurements downstream of wind farms are typically limited to the prevailing wind direction. At the offshore wind farm Vindeby, Denmark three meteorological masts have been arranged near 11 wind turbines such that simultaneous measurements of wind speed in the free stream and wake were obtained for several wind directions (Frandsen et al., 1996; Frandsen & Thomsen, 1997). Measurements were made at fixed and relatively short distances from the turbines (i.e. up to 1.4 km). To obtain measurements at various distances downstream from the turbines at Vindeby, velocity profiles were obtained with Sonic Detection and Ranging (SODAR) from a ship (Barthelmie et al., 2003, 2004b). In the experiment, free stream conditions were achieved by turning off the wind turbines while a second set of velocity profiles were measured.

The experiments described above have quantified wake effects from a single turbine and multiple turbines aligned in one row. Wake effects of large turbine arrays are far more complex as single wakes start interacting with other wakes

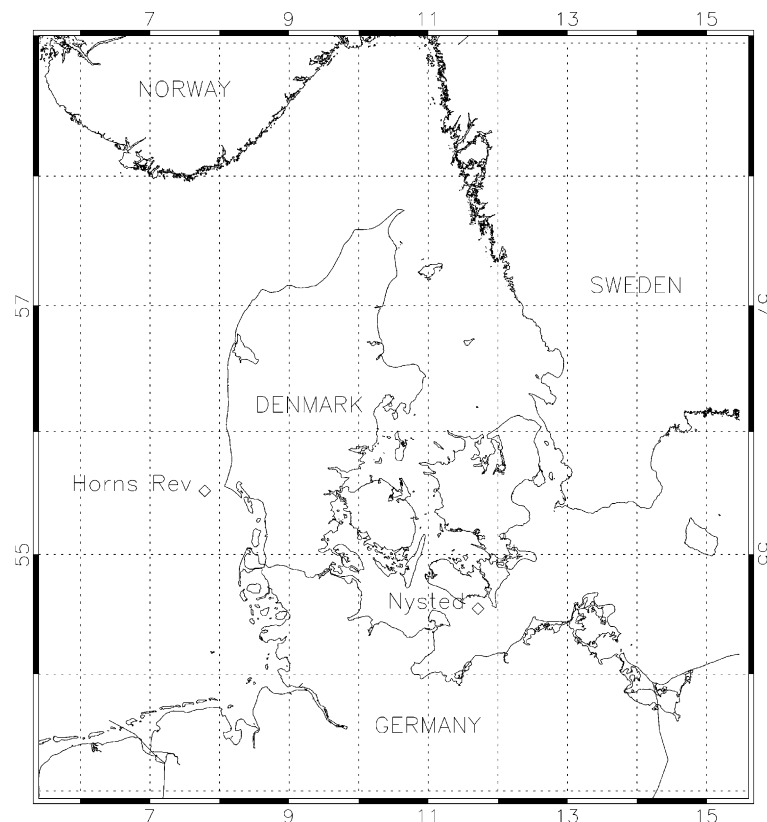


Fig. 2. Map of Denmark showing the location of the offshore wind farms at Horns Rev and Nysted.

downstream at e.g. 30 rotor diameters (Frandsen et al., 2004). Wakes from large offshore wind farms have been modeled (Barthelmie et al., 2004c; Crespo et al., 1999; Frandsen et al., 2004). Wake models estimate wake deficits of 12–16% downstream of large offshore wind farms and that the wind recovers to within 2% of its ambient speed over a downstream distance of 5–14 km (Barthelmie et al., 2004a; Barthelmie & Pryor, in press).

The hub-height turbulence intensity increases downwind of wind turbines. Frandsen and Christensen (1994) have reported an increased standard deviation of the wind speed in the wake at hub-height of 10–35 %. Maximum standard deviations occurred at low wind speeds ($3\text{--}10\text{ m s}^{-1}$). At 10 m above sea level, the change of standard deviation from the upstream to the downstream side of wind turbines was much smaller. At high wind speeds ($12\text{--}14\text{ m s}^{-1}$), a decrease of standard deviation was measured.

5. Study sites and data

The present study is carried out at the two Danish wind farm sites indicated in Fig. 2: Horns Rev in the North Sea and Nysted in the Baltic Sea. At Horns Rev, an array of 80 wind turbines, each with a capacity of 2 MW, is located 14–20 km offshore (Fig. 3a). The wind farm is built on a submerged reef at water depths of 5–15 m and with a distance of 560 m between individual turbines. Turbine hub-heights are 70 m and the rotor diameter is 80 m, hence the maximum height of blade tips is 110 m above mean sea level. Data provided by Elsam Engineering A/S show that, at any given time, a fraction of the turbines may be non-operational due to scheduled regulation of the power output, maintenance, or technical problems. An offshore meteorological mast is located to the northwest of the wind farm as indicated in Fig. 3a. For this study, the following measurements have been extracted as mean values over 10 min intervals: wind direction (60 m), wind speed (15 and 62 m), turbulence intensity (62 m), and air temperature (13 and 55 m). A total of 34 SAR scenes have been acquired and purchased since the wind farm became operative in December 2002; 25 of the scenes are from ERS-2 and 9 from Envisat (Table 1).

Nysted Offshore Wind Farm is located 10 km south of the island Lolland and 13 km west of the island Falster. Fig. 3b shows the outline of the wind farm. It consists of 72 turbines, each with a capacity of 2.3 MW, built near two sand bars where water depths are 6–9.5 m. Each turbine has a hub-height of 68.8 m, a rotor diameter of 82.4 m, and a maximum height of blade tips of 110 m above mean sea level. The turbines are spaced 867 m apart in the east–west direction and 481 m in the north–south direction. We have purchased 7 SAR scenes after the wind farm became operational in December 2003: a

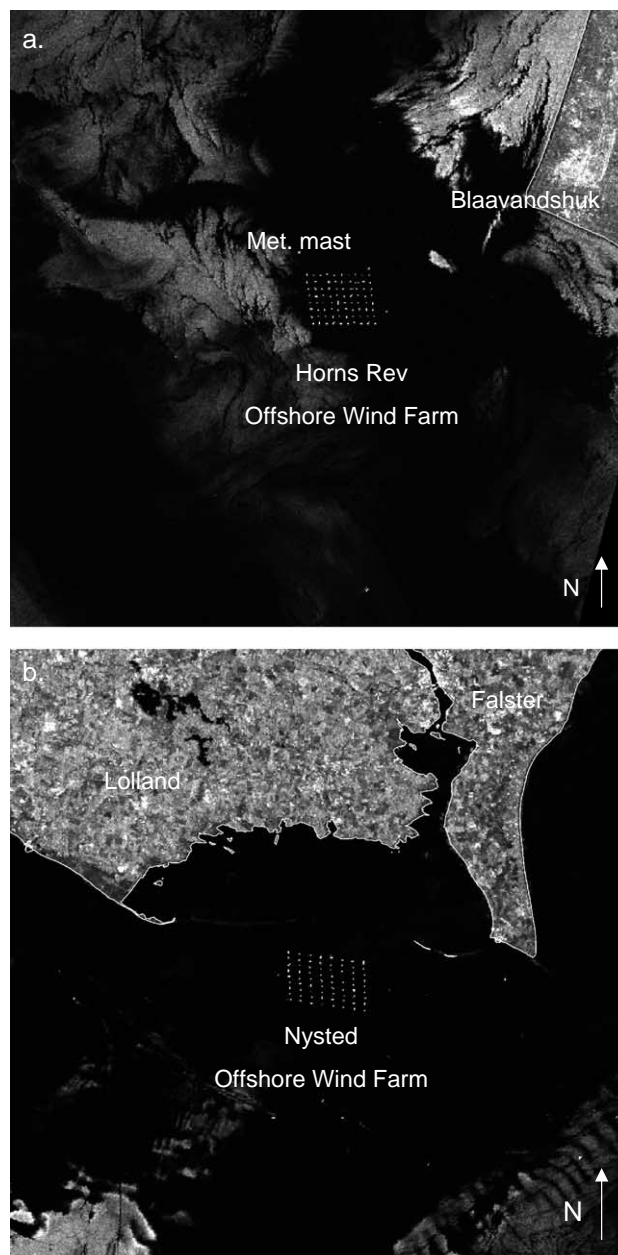


Fig. 3. Subsection of ERS-2 backscatter images (50 by 50 km) showing the configuration of wind turbines at (a) Horns Rev (29 May 2003), and (b) Nysted (17 August 2004) under calm conditions. Bright areas offshore are not associated with wind generated surface roughness.

total of 5 scenes are from ERS-2 and 2 are from Envisat (Table 1).

6. Method

6.1. Quality control

Three of the SAR scenes listed in Table 1 display large-scale meteorological features (e.g. rain cells), which hamper the generation of reliable wind speed maps. Through inspection of all the wind maps, it also becomes

Table 1

Available ERS-2 SAR and Envisat ASAR scenes and in situ measurements of turbulence intensity and wind speed for Horns Rev (hourly at 62 m)

Date (ddmmyy)	Time (UTC)	Satellite	Product	Location	Turbulence int. (%)	Wind speed (m s ⁻¹)	Wind direction
171202	10:26	ERS-2	PRI	Horns Rev	–	2.0	17
050103	10:29	ERS-2	PRI	Horns Rev	14.0	11.2	320
090203	10:29	ERS-2	PRI	Horns Rev	9.0	11.2	162
100203	21:22	ERS-2	PRI	Horns Rev	8.4	8.3	151
220203	21:17	Envisat	APP	Horns Rev	9.5	9.5	126
250203	10:26	ERS-2	PRI	Horns Rev	6.0	6.0	110
010303	21:25	ERS-2	PRI	Horns Rev	7.3	8.6	124
160303	10:29	ERS-2	PRI	Horns Rev	6.9	2.1	255
200303	21:28	ERS-2	PRI	Horns Rev	9.8	8.0	136
010403	10:26	ERS-2	PRI	Horns Rev	8.3	13.0	196
200403	10:29	ERS-2	PRI	Horns Rev	12.0	11.7	114
210403	21:22	ERS-2	PRI	Horns Rev	7.2	8.8	104
060503	10:26	ERS-2	PRI	Horns Rev	6.9	5.9	238
100503	21:25	ERS-2	PRI	Horns Rev	7.2	3.7	196
250503	10:29	ERS-2	PRI	Horns Rev	10.5	4.0	134
290503	21:28	ERS-2	PRI	Horns Rev	15.6	1.8	331
100603	10:26	ERS-2	PRI	Horns Rev	9.0	4.9	137
140603	20:57	Envisat	APP	Horns Rev	8.0	6.8	330
170603	09:38	Envisat	APP	Horns Rev	–	0.0	135
290603	10:29	ERS-2	PRI	Horns Rev	15.2	6.4	53
300603	20:54	Envisat	APP	Horns Rev	10.4	8.6	120
300603	21:22	ERS-2	PRI	Horns Rev	10.0	8.1	105
040803	20:54	Envisat	APP	Horns Rev	8.0	4.6	2
070803	21:28	ERS-2	PRI	Horns Rev	8.7	6.7	27
190803	10:26	ERS-2	PRI	Horns Rev	8.6	8.3	279
230903	09:58	Envisat	APP	Horns Rev	10.1	14.1	297
091003	09:55	Envisat	APP	Horns Rev	9.6	12.5	312
121003	10:29	ERS-2	PRI	Horns Rev	8.8	9.2	331
071103	10:12	ERS-2	PRI	Nysted	–	–	75
161103	10:29	ERS-2	PRI	Horns Rev	6.9	6.4	247
021203	10:26	ERS-2	PRI	Horns Rev	9.5	9.5	106
061203	21:25	ERS-2	PRI	Horns Rev	17.4	7.1	48
161203	20:42	Envisat	IMP	Nysted	–	–	241
211203	10:29	ERS-2	PRI	Horns Rev	12.0	9.8	97
200104	20:42	Envisat	IMP	Nysted	–	–	355
010204	10:09	ERS-2	PRI	Nysted	–	–	325
040404	10:01	Envisat	IMP	Horns Rev	–	7.0	204
110404	10:09	ERS-2	PRI	Nysted	–	–	275
180404	21:14	ERS-2	PRI	Nysted	–	–	115
240404	20:57	Envisat	IMP	Horns Rev	–	2.0	350
170804	11:37	ERS-2	PRI	Nysted	–	–	–

Also listed are the wind directions chosen as input to CMOD-4 in degrees north (– data not available).

clear that bathymetry, particularly the submerged reef on which the Horns Rev wind farm is built, affects the surface roughness, contaminating wind retrievals from the radar signal. An example is shown in Figs. 4 and 5 where a subsection of an ERS-2 scene is compared to a corresponding bathymetry map of Horns Rev. The submerged reef has a curved outline, which is recognized both in the SAR image and on the bathymetry map. Bathymetry is less evident in images from the Nysted site. Whenever effects of bathymetry coincide in space with the wake downstream of a wind farm, scenes are eliminated. Other scenes are eliminated because the wind farm wake exceed the image boundary. Finally, scenes are eliminated for winds below the cut-in wind speed. A total of 19 scenes remain for the study of wind wakes (Table 2).

6.2. SAR wind retrieval

ERS-2 SAR and ENVISAT ASAR scenes are calibrated to σ^0 using the BEST software tool from the European Space Agency (ESA). All images are geographically rectified using the corner coordinates provided in the data files. A mask is defined to remove image pixels contaminated by direct scattering from wind turbines. Due to layover and radar shadowing effects, scattering from a single wind turbine affects several nearby pixels. Some pixels contain scattering from both turbine and sea surface, therefore pixels are eliminated according to their location (i.e. around each turbine) rather than their backscatter coefficient. More specifically, pixels that are partly or fully located within a 100 m radius from each of the turbines are masked out. Remaining pixels are averaged to 400 m to reduce speckle noise.

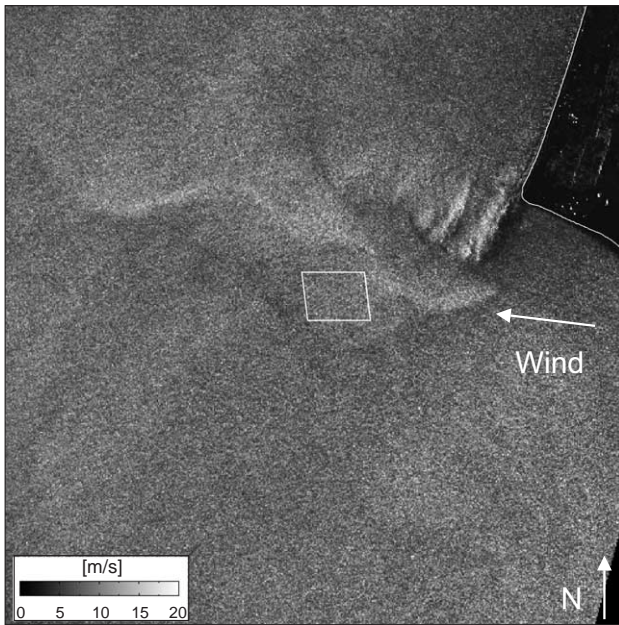


Fig. 4. Wind speed map based on subsection (50 km by 50 km) of the ERS-2 SAR scene of 21 December 2003. The wind farm at Horns Rev is indicated (white trapezoid) and the submerged reef is visible. Wind direction = 97° , wind speed = 8.8 m s^{-1} from mast.

Selection of appropriate wind directions for CMOD-4 input is based on meteorological measurements (Horns Rev only), and indications of wind direction in the images

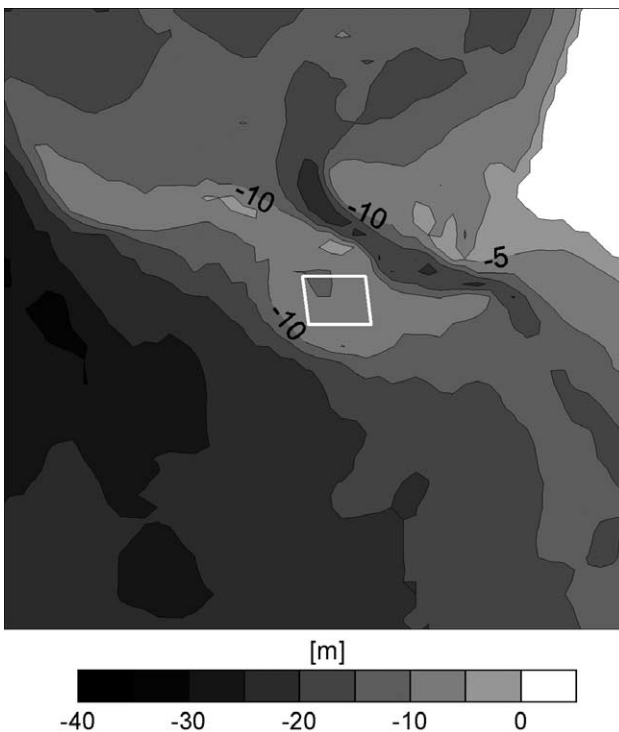


Fig. 5. Bathymetry map covering the area of the SAR image in Fig. 4. The wind farm at Horns Rev is indicated (white trapezoid). Courtesy DHI/50395/2.ed.Nov 2001/PH/KAE.

Table 2

Summary of scene characteristics

Scene characteristic	Number of scenes
Suitable for wake study	19
$U < \text{cut-in wind speed}$	6
$U > \text{nominal wind speed}$	0
Bathymetric effects	10
Atmospheric effects	3
Image boundary exceeded	3
Total	41

e.g. streaks and wind shadows. Meteorological measurements are 10-minute averages. In contrast, the SAR scenes are snapshots captured over few seconds. To eliminate fluctuations, hourly averages of the measured wind directions, centred at the time of each satellite pass, are used as in Hasager et al. (2004b, in press) unless a trend of increasing or decreasing wind speed over time is observed. When in situ wind directions are unavailable or fail to align with streaks or wind shadows, directions are obtained from the image. Table 1 lists the chosen wind directions. Finally, the CMOD-4 (Eq. (1)) is inverted to produce wind speed maps.

6.3. Velocity deficit

Spatial averages of wind speed are extracted from the SAR wind maps using two transects of boxes aligned with the wind vector as outlined in Fig. 6 (black). One transect crosses the wind farm, either at Horns Rev or Nysted, and is denoted the *wake* transect. An identical transect is outlined

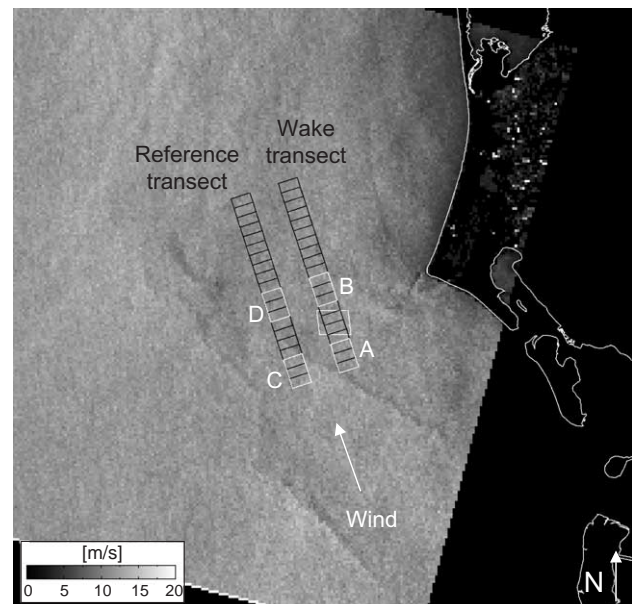


Fig. 6. Wind speed map based on the ERS-2 scene captured on 09 February 2003. The following is indicated: Horns Rev Offshore Wind Farm (white trapezoid), two transects parallel to the wind direction (black), and box A–D (white). Wind direction = 162° , wind speed = 11.2 m s^{-1} from mast.

parallel to the former transect, but with a displacement of 8 km to provide reference measurements from the non-obstructed flow. This transect is denoted the *reference* transect. The total extent of each transect in the direction of the wind is 32 km. The wake transect extends 4.0 km upwind and 20.8 km downwind of the wind farms. We define the wind farm extent (7.2 km) from the maximum distance that can contain turbines at any given wind direction.

Since we intend to capture the wake phenomena and not the area surrounding it, there is an upper limit to the desired width of transects. Yet, wakes are constantly shifting with the wind direction and narrow boxes could fail to capture the wake effect. From this, we choose the width of each box as 3.2 km (8 pixels). The length of each box, aligned with the wind, is 1.6 km. Hence, individual boxes contain approximately 40 pixels, which ensures a standard deviation of wind speed of $\sim 0.5 \text{ m s}^{-1}$ and $\pm 1 \text{ m s}^{-1}$ at the 95% confidence interval. Extraction of average wind speeds within boxes is performed as a moving average such that a value is extracted per 0.4 km (a quarter of a box) along the two transects. Spatial averages of wind speed are used to calculate velocity deficits in the vicinity of the wind farms. Eq. (2) is applied in two forms for each SAR scene.

Following a classical meteorological approach, wind speeds in the wake are normalized with the free stream velocity obtained upstream of wind farms. Practically, U_{wake} is wind speed obtained for boxes along the wake transect. $U_{\text{freestream}}$ is the average wind speed in three boxes upstream of the wind farms (area A in Fig. 6). The resulting velocity deficit is denoted VD.

SAR wind speed maps facilitate a new, alternative approach where free stream wind speeds are obtained from the reference transect aligned parallel to the wake transect. U_{ref} is the wind speed measured at distances corresponding to U_{wake} , but in the reference transect. The resulting reference velocity deficit is denoted VD_{ref} . The new method eliminates uncertainties related to general increases or decreases of wind speed in coastal regions. It has been shown (Barthelmie et al., 2004a; Hasager et al., 2004a; Nielsen et al., 2004) that winds in the coastal zone may have significant spatial gradients within the distances under study.

6.4. Atmospheric stability

To estimate the atmospheric stability during each satellite pass, we calculate the bulk Richardson number, Ri_B :

$$Ri_B = \frac{g}{T} \frac{[\theta(z_1) - \theta(z_2)]/(z_1 - z_2)}{([u(z_3) - u(z_4)]/(z_3 - z_4))^2} \quad (4)$$

where g is acceleration of gravity, T (K) is absolute temperature at a given height (z_1 in our case) and θ (K) is potential temperature, which is derived from T using the

adiabatic lapse rate (-0.01 K m^{-1}). Measurements are obtained at $z_1=55 \text{ m}$, $z_2=13 \text{ m}$, $z_3=62 \text{ m}$, and $z_4=15 \text{ m}$ at Horns Rev. Estimates of atmospheric stability are valid at 55 m when these measurement heights are used. The following intervals are defined: $Ri_B < -0.4$ for unstable atmospheres, $-0.4 \leq Ri_B \leq 0.1$ for near-neutral atmospheres, and $Ri_B > 0.1$ for stable atmospheres.

6.5. Turbulence intensity

Turbulence intensity (I) is calculated from Eq. (3) using data obtained within each of the four boxes A–D shown in Fig. 6 (white). I_A is the result for box A, I_B for box B etc. Each box contains approximately 100 pixels and covers an area of 3.2 km by 4.8 km. The difference in turbulence intensity upstream (I_A) and downstream (I_B) of the wind farm is ΔI . In the coastal zone, variations in turbulence intensity occur analogous to fetch-induced wind speed variations. Therefore, a reference turbulence intensity difference is defined as $\Delta I_{\text{ref}} = I_C - I_D$. Finally, ΔI is corrected through subtraction of ΔI_{ref} to yield the turbulence intensity added by wind turbines, I_{added} .

7. Results

7.1. Noise floor

Speckle noise is associated with any coherent measurement. Such noise in SAR imagery is generally reduced by multi-look processing or by averaging higher resolution pixels. In calculating wind speed variance from SAR imagery it is important to discriminate between true wind speed variance and apparent wind speed variance caused by speckle (Ulaby et al., 1982). The radiometric resolution (Q) in SAR images is described in dB by the signal-to-noise ratio:

$$Q = 10 \log \left(1 + \frac{1}{\sqrt{\text{ENL}}} \right) \quad (5)$$

where ENL is the equivalent number of looks, which increases with the number of pixels averaged. The speckle noise floor is compared for the three different product types studied (ERS-2, Envisat APP mode, and Envisat IMG mode). Values of ENL and Q are shown in Table 3. The

Table 3
Equivalent number of looks (ENL) and radiometric resolution (Q) for the three SAR image types used

Satellite	Product	ENL		Q [dB]
		25 m	400 m	400 m
ENVISAT	APP	~ 2	215	0.29
ERS-2	PRI	~ 3	441	0.20
ENVISAT	IMG	~ 4	533	0.18

signal-to-noise ratio ranges 0.2–0.3 dB. According to Stoffelen and Anderson (1997b), ± 0.2 dB corresponds to an uncertainty in wind speed retrievals of $\sim 0.5 \text{ m s}^{-1}$. The uncertainty is reduced as we average over larger SAR image areas.

7.2. Wind speed maps

A SAR wind speed map over Horns Rev is shown in Fig. 7. The map is based on the ERS-2 SAR scene of 25 February 2003. The wind direction is 110° relative to north as indicated by wind streaks and wind shadows. A wake is seen as a dark elongated area extending from the wind farm and westward. At the image boundary, approximately 20 km downstream, there is still a significant velocity deficit compared to the area surrounding the wake. Wake phenomena are also recognized leeward of coastal dunes. Although the dunes are less than 30 m above mean sea level, they create much higher velocity deficits than the wind turbines. The wind speed map shows a general increase of wind speed with distance from the shoreline.

Scattering from wind turbines is very distinct in SAR scenes captured under calm ($< 2 \text{ m s}^{-1}$) conditions as seen in Fig. 3a for Horns Rev and Fig. 3b for Nysted. At higher wind speeds, individual wind turbines are difficult to distinguish in SAR images and it becomes difficult to check that the mask we have defined is accurately positioned over the turbines. Wind speeds inside both wind farms are always lowered by the mask but turbine scattering may not be totally removed.

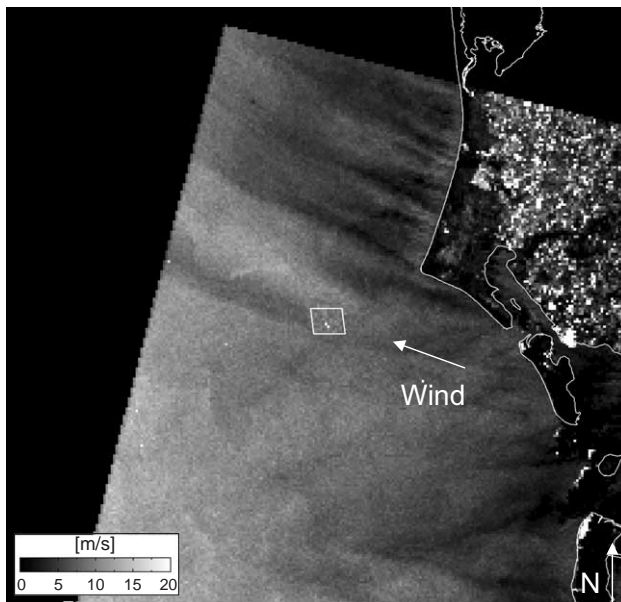


Fig. 7. Wind speed map based on the ERS-2 scene captured on 25 February 2003. The wind farm at Horns Rev is indicated (white trapezoid) and a wind wake is seen as dark pixels downstream of the turbines. Wind direction = 110° , wind speed = 6.0 m s^{-1} from mast.

7.3. Velocity deficit

In Fig. 8a and b, velocity deficit (VD) for all individual transects is shown. VD is positive when measured wind speeds (U_{wake}) are below the free stream velocity ($U_{\text{freestream}}$). We set $\text{VD} = 2\%$ as the threshold for wake occurrence. Results for onshore winds (7 cases) and offshore winds (12 cases) are separated. In our case, onshore winds are the fetch-unlimited whereas offshore winds are the fetch-limited directions.

For onshore winds, increasingly positive values of VD are found with distance into the wind farm for four SAR scenes. Three other scenes show negative values within the wind farm. For 12 October 2003, VD is -17% . This may be the residual effect of turbine scattering. Immediately downstream of the wind farm, all transects show a positive VD. In the first downstream box free of turbines (0–1.6 km), VD ranges 0–20%. VD continues to grow with distance for five transects, whereas it remains constant or declines for the others. For 09 October and 12 October 2003, VD reaches 2% at downstream distances of 7 and 12 km, respectively. For all other transects, VD remains above 2% over the downstream distance studied (21 km).

For offshore winds, seven SAR scenes show an increasing VD with distance into the wind farms. For these cases, VD peaks shortly after the last turbine (0–3.2 km) at 30% or lower. Further downstream, VD decreases. All cases except one (02 December 2003) show VD below 10% at 21 km. VD is negative throughout the transects for five cases, down to -72% for 29 June 2003.

The average VD for onshore and offshore transects are shown in Fig. 8c. For onshore winds, a rapid increase of VD is seen over the wind farms. The deficit measured just downstream of the farms is 11% on average. The maximum VD is 13% at 3 km downstream of the last turbine, then VD drops to a constant value of $\sim 11\%$. For offshore winds, the average VD also increases over the wind farms but at a slower rate than for onshore winds. A global maximum deficit of 4% is found where the wind farms end. VD decreases to 2% at 2 km and to -10% at 21 km downstream.

Fig. 9a and b show reference velocity deficits (VD_{ref}) for all individual transects grouped as onshore and offshore winds. VD_{ref} is positive when measured wind speeds (U_{wake}) are below the corresponding free stream velocities (U_{ref}) obtained from the non-obstructed reference transect (cf. Section 6.3). The new, alternative reference method is based on the premise that U_{wake} equals U_{ref} upstream of the two wind farms. We consider variations below $\pm 15\%$ acceptable.

For onshore winds, VD_{ref} is within $\pm 15\%$ upstream of the wind farms for all seven transects. As for the previous reference method, negative velocity deficits occur within the wind farms, possibly as a residual effect of wind turbine scattering. Positive VD_{ref} values are found for all cases,

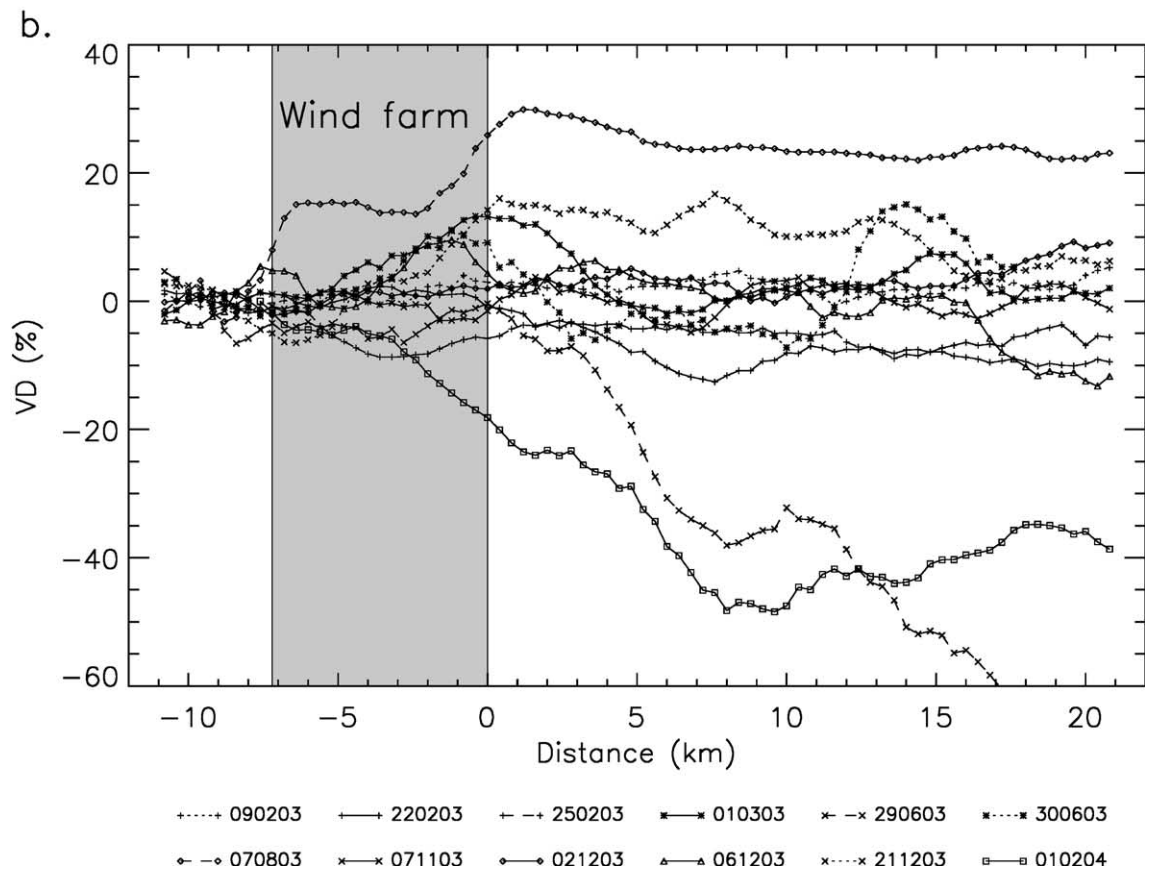
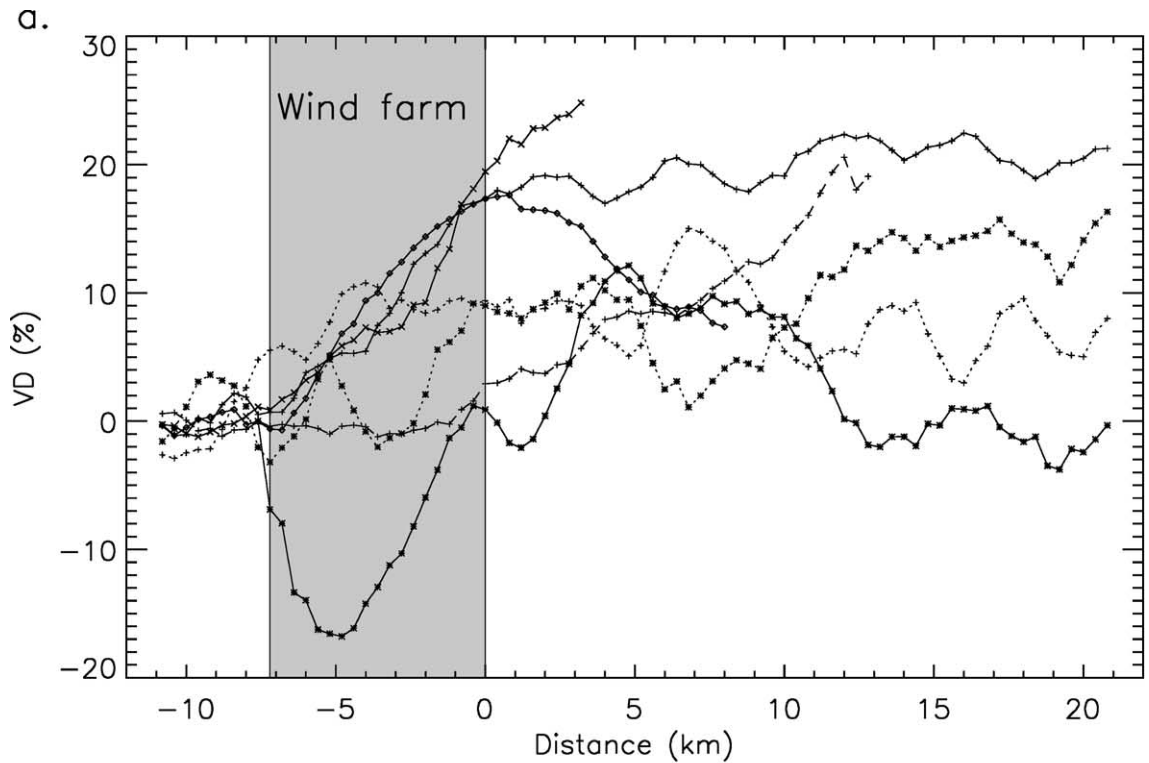


Fig. 8. Velocity deficit (VD) for SAR scenes (ddmmyy) captured with (a) onshore winds, and (b) offshore winds. Line signatures show intervals of the SAR free stream velocity: $U < 6 \text{ m s}^{-1}$ (dashed), $6 \text{ m s}^{-1} \leq U < 9 \text{ m s}^{-1}$ (solid), and $U \geq 9 \text{ m s}^{-1}$ (dotted). (c) Shows average VD for onshore and offshore winds.

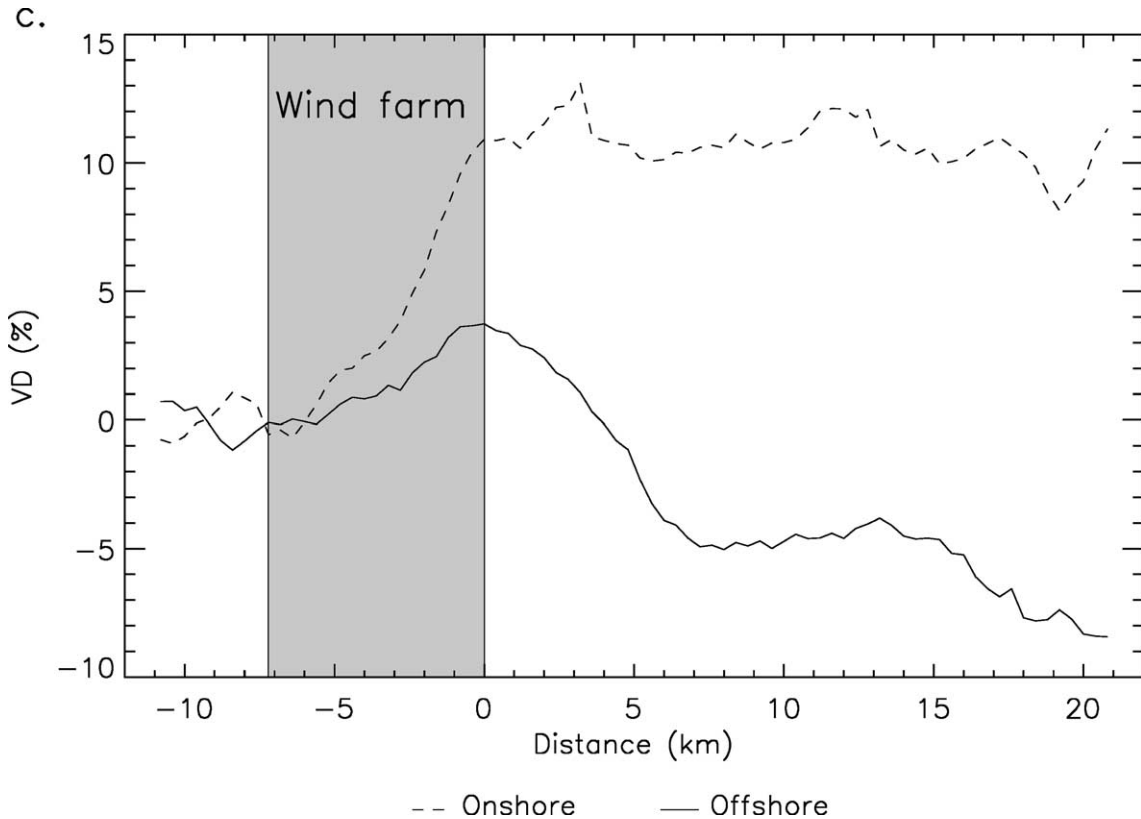


Fig. 8 (continued).

eventually. VD_{ref} peaks at various distances from 0 to 14 km downstream of the wind farms.

For offshore winds, VD_{ref} fails to be within $\pm 15\%$ upstream of the wind farms in two cases (29 June and 21 December 2003). The two scenes are eliminated from further analysis and interpretation with respect to VD_{ref} . Flow patterns are complex but generally, VD_{ref} increases over the wind farms. VD_{ref} measured within the first downstream box free of turbines (0–1.6 km) range from 0% to 33%. VD_{ref} is below 15% for all cases at the downstream distance 21 km.

Average VD_{ref} plots for onshore and offshore cases separated are shown in Fig. 9c. The upstream values of VD_{ref} varies between -3% and 7% . A striking feature is the similarity of VD_{ref} in the wake region. This is in contrast to the divergent curves in Fig. 8c. VD_{ref} for onshore cases peaks at $\sim 8\%$ both 3 and 11 km downstream, whereas VD_{ref} for offshore cases peaks at 9% 1 km downstream and again at 7% 15 km downstream. For onshore winds, VD_{ref} is above 2% for the downstream distance 0–18 km. For offshore winds, values below 2% are reached at 7–9 km, before the second peak of VD_{ref} .

Velocity deficits are compared to three factors that presumably have an impact on the magnitude of wake effects from wind farms: the free stream velocity, the atmospheric stability, and the number of turbines in operation. Line signatures in Fig. 8 (a, b) and Fig. 9 (a, b) indicate intervals of the SAR-derived free stream velocity:

$U_{freestream} < 6 \text{ m s}^{-1}$ (dashed), $6 \text{ m s}^{-1} \leq U_{freestream} < 9 \text{ m s}^{-1}$ (solid) and $U_{freestream} \geq 9 \text{ m s}^{-1}$ (dotted). The free stream velocities are obtained upstream of the wind farms as in the calculation of VD . In Table 4, $U_{freestream}$ and VD_{ref} obtained within the first box downstream of the wind farms in the wake transect are listed. VD_{ref} exceeds 15% for free stream velocities of $4.8\text{--}6.9 \text{ m s}^{-1}$. VD_{ref} values of $10\text{--}15\%$ are found for almost the same range of free stream velocities ($4.8\text{--}6.8 \text{ m s}^{-1}$), whereas deficits of $0\text{--}10\%$ are observed for a wider range of free stream velocities ($4.7\text{--}11.9 \text{ m s}^{-1}$).

The bulk Richardson numbers (Ri_B) calculated from Eq. (4) are listed in Table 4. Ri_B indicates unstable conditions for three cases. For six cases, Ri_B indicates near-neutral atmospheric stability. In addition, three cases with $U_{freestream} > 8 \text{ m s}^{-1}$ are assumed near-neutral (air temperatures are unavailable). Fig. 10 shows VD_{ref} averaged for near-neutral and unstable cases, separately. VD_{ref} is similar upstream of the wind farms with values below 6% . For near-neutral cases, VD_{ref} increases within the wind farms to 8% near the downstream wind farm boundary. VD_{ref} fluctuates between 2% and 9% up to 19 km downstream. At the far downstream end of transect, VD_{ref} is below 2% . For unstable cases, fluctuations of VD_{ref} occur within the wind farms. In the wake region, VD_{ref} peaks at 8% approximately 1 km downstream of the last wind turbine. From this point, a rapid decrease of VD_{ref} is found, reaching 2% at only 5 km downstream.

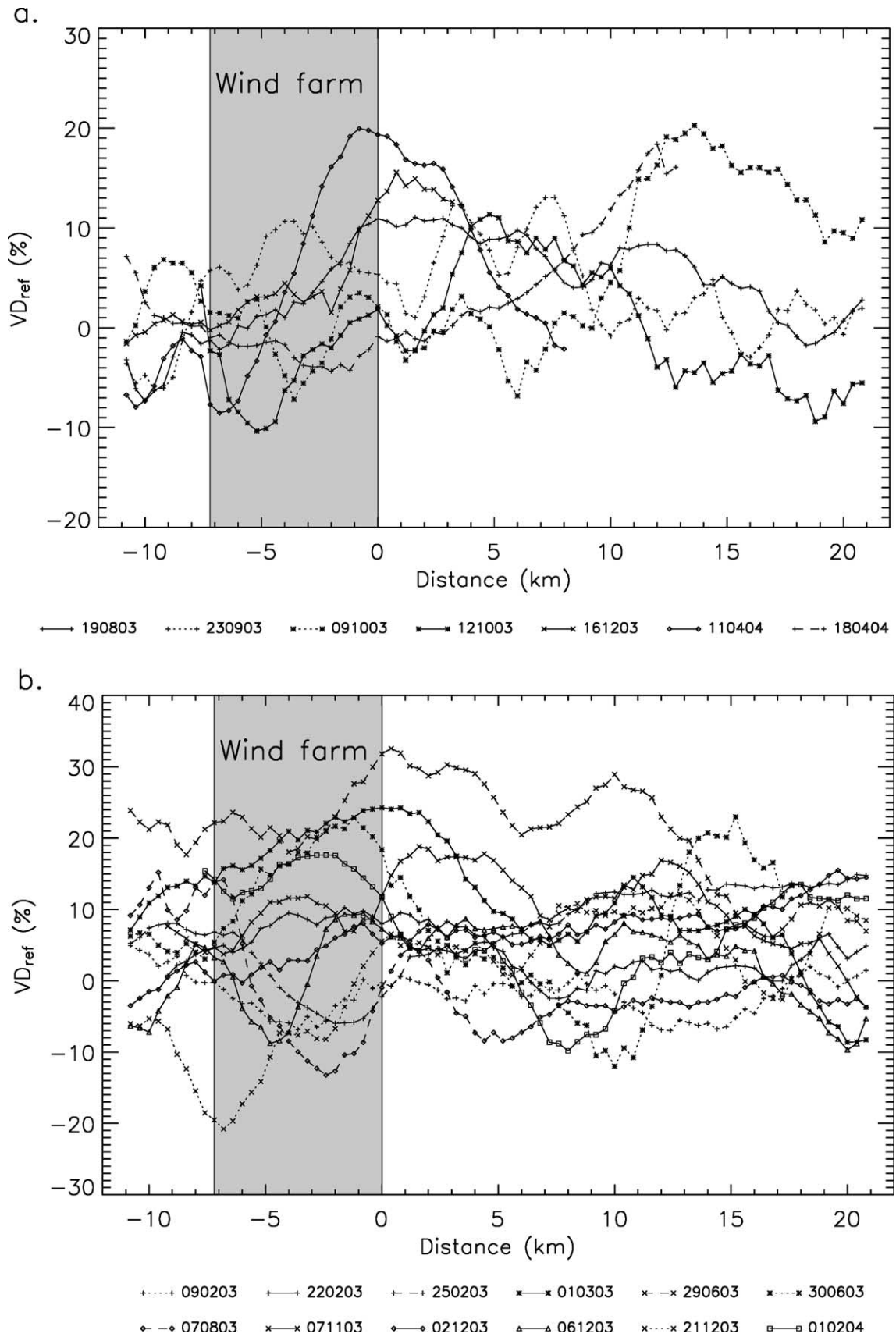


Fig. 9. Reference velocity deficit (VD_{ref}) for SAR scenes (ddmmyy) captured with (a) onshore winds, and (b) offshore winds. Line signatures show intervals of the SAR free stream velocity: $U < 6 \text{ m s}^{-1}$ (dashed), $6 \text{ m s}^{-1} \leq U < 9 \text{ m s}^{-1}$ (solid), and $U \geq 9 \text{ m s}^{-1}$ (dotted). (c) Shows average VD_{ref} for onshore and offshore winds.

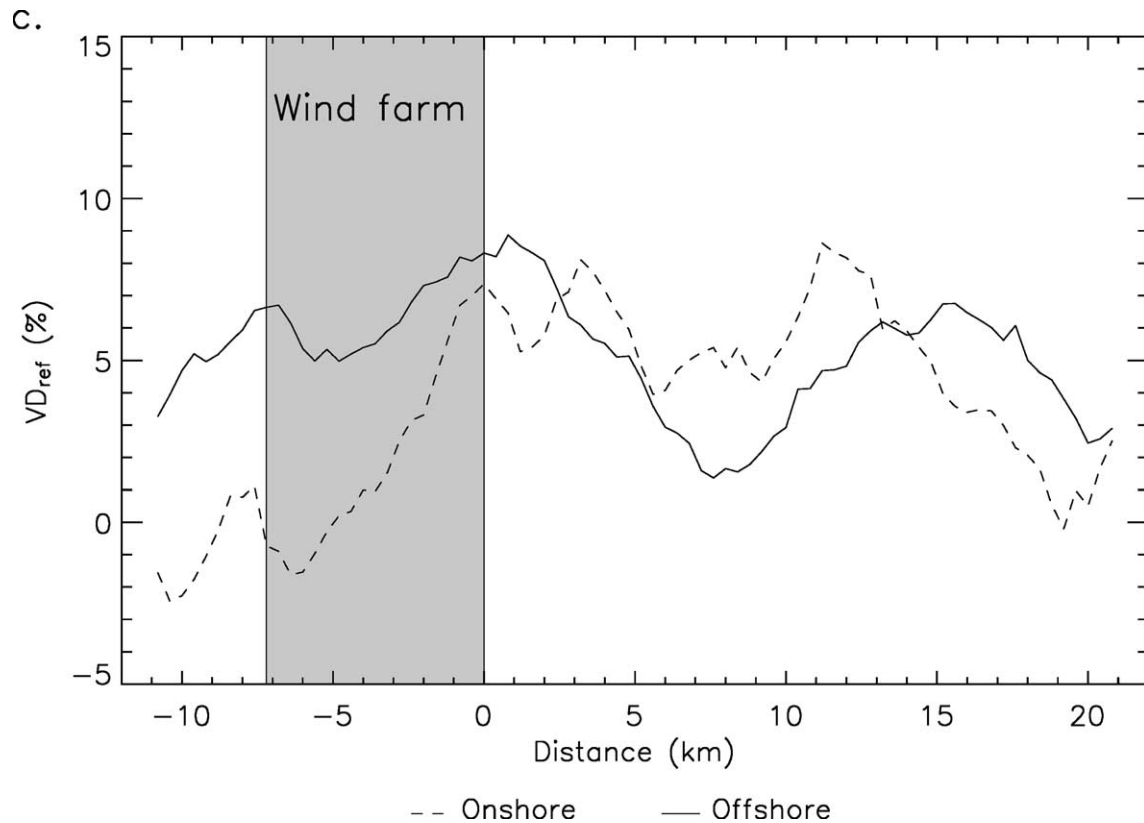


Fig. 9 (continued).

The number of wind turbines in operation during each satellite pass is known for Horns Rev (Table 4). Generally, a large portion of the turbines at Horns Rev

are running and significant wake effects observed. Surprisingly, VD_{ref} is ~11% for 19 August 2003 although only 6 turbines are operating. It is assumed, that most

Table 4
ERS-2 and Envisat scenes analyzed for wake effects

Date (ddmmyy)	Turbines	Ri_B	$U_{\text{freestream}}$ (m s^{-1})	VD _{ref} (%)	ΔI (%)	ΔI_{ref} (%)	I_{added} (%)
<i>Onshore winds</i>							
190803	6	-1.09	6.5	10.7	-1.1	0.8	-0.2
230903	60	-	11.9	4.5	1.0	-4.9	-3.8
091003	67	-	10.6	1.3	0.7	-0.9	-0.2
121003	64	-	6.7	0.2	-	-	-
161203	-	-	4.8	13.7	1.0	-0.1	0.9
110404	-	-	6.6	19.2	1.7	8.0	9.7
180404	-	-	5.9	-1.3	0.7	-0.8	-0.1
<i>Offshore winds</i>							
090203	26	-0.20	12.5	-0.8	-0.3	1.7	1.4
220203	62	-7.52	8.2	8.5	1.1	-0.3	0.8
250203	43	0.04	4.2	-0.7	1.2	0.0	1.2
010303	37	-0.23	6.9	24.1	1.0	1.3	2.3
290603**	-	-0.23	4.8	32.6	-3.5	2.3	-1.2
300603*	51	-0.37	6.8	13.4	2.5	-0.5	2.0
070803	61	-6680	4.7	1.4	-	-	-
071103	-	-	5.9	14.8	-1.7	-1.9	-3.6
021203	38	-	7.9	6.2	3.8	0.8	4.6
061203	50	-0.12	6.5	6.2	-3.4	0.4	-3.0
211203**	42	-	9.1	6.6	-	-	-
010204	-	-	6.3	9.0	-1.9	0.2	-1.7

*The pass at 20:54 UTC, **eliminated (VD_{ref}>15% upstream of wind farm).

The number of turbines in operation and the bulk Richardson number (Ri_B) are listed along with results gained from SAR images: $U_{\text{freestream}}$, VD_{ref}, ΔI , ΔI_{ref} , and I_{added} . See text for definitions (- data not available).

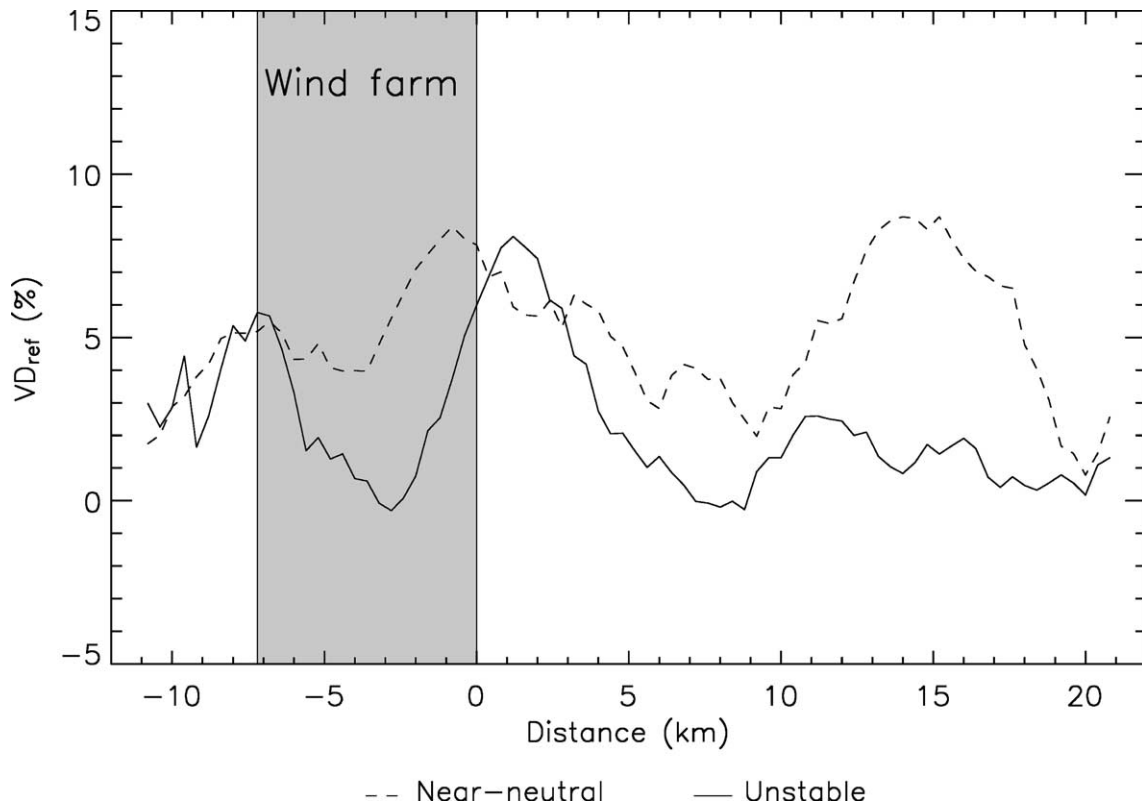


Fig. 10. Average reference velocity deficit (VD_{ref}) for SAR scenes acquired with unstable and near-neutral atmospheric stability.

turbines at Nysted are running (R. Barthelmie, personal communication).

7.4. Turbulence intensity

ΔI , ΔI_{ref} and I_{added} are listed in Table 4. Turbulence intensity found from the SAR images is generally comparable to values measured at the offshore mast at Horns Rev (Table 1). With onshore winds, ΔI is between -1.1% and 1.7% . Correction using ΔI_{ref} is important where downstream variations of ambient turbulence intensity are found (I_C differ from I_D). However, I_{added} can only be successfully determined if turbulence intensity measured upstream of a wind farm (I_A) is equivalent to turbulence intensity measured in the corresponding box of reference (I_C). This is not the case for 23 September 2003 and 11 April 2004. For the other cases obtained with onshore winds, corrections within $\pm 1\%$ point are made, leading to I_{added} ranging from -0.2% to 0.9% .

Scenes captured with offshore winds show a larger variability of ΔI from -3.5 to 3.8% . ΔI is positive for five scenes and negative for five other scenes. For 09 February 2003, correction with ΔI_{ref} transforms a negative ΔI to a positive I_{added} . Positive values of I_{added} are found for a total of six scenes and negative I_{added} for four scenes. Values of I_{added} are between -3.6% and 4.6% , thus the effect of correction is small.

8. Discussion

The aim of our study is to identify wake effects near two large offshore wind farms from satellite SAR data. We have demonstrated that wind farm wakes are visible on SAR wind speed maps (Fig. 7). To quantify the wake effect, velocity deficit and turbulence intensity have been found from a total of 19 SAR scenes. Key results and interpretations are provided in the following discussion.

8.1. Wind speed maps

Wind fields have been successfully derived from SAR images using the geophysical model function CMOD-4. Some issues must be considered when the model function is applied in near-shore areas, areas that are preferred for offshore wind farming. A logarithmic wind profile is assumed in the derivation of wind speed from SAR. In the coastal zone, deviations from the logarithmic wind profile can occur due to non-neutral stability (Barthelmie, 1999), the presence of internal boundary layers (Garratt, 1990), or horizontal advection of air (Lange et al., 2004). Non-neutral conditions typically occur at low wind speeds whereas the marine atmosphere is near-neutral for wind speeds above 8 m s^{-1} . For unstable conditions, winds at 10 m may be overestimated if not corrected. No correction has been applied in the present study. Stable conditions have not been observed in our dataset.

Wind turbines generate turbulence such that the air downstream of the turbines is well mixed. Maximum velocity deficit and turbulence intensity are found near hub-height (Frandsen & Christensen, 1994). At the surface, wakes are weaker, but not altogether absent. Analogous to the over-estimation of wind speeds for unstable conditions, 10 m wind speeds may be over-estimated due to the mixing of air caused by wind turbines. In addition, turbulence in the wake of offshore wind farms may change the sea surface roughness and lead to some bias in wind retrievals from SAR. Within offshore wind farms, there is a possibility of wave refraction generated by the turbine towers. Refracted waves may also impact on surface roughness and thus on the SAR backscatter coefficient. Since the tower diameter is small (5 m) compared to the turbine spacing, we believe this effect is small.

Our study shows that high radar backscattering from wind turbines can be successfully removed by excluding pixels surrounding each wind turbine before wind retrieval. Removal of turbine scattering is most efficient on calm days when there is a high contrast between sea surface and turbine scattering. At higher wind speeds, the gradient of σ^0 tends to decrease.

Automatic retrieval of wind direction from SAR images is a key research topic (cf. Section 3). Only 19 cases are studied here, hence inspection of individual scenes is possible. In addition, offshore meteorological observations are available for most cases. Wind directions obtained from the mast at Horns Rev and image features differ with less than 10° except for two cases showing deviations of $\sim 25^\circ$. The principle reason for this deviation is that meteorological measurements are averaged over time (i.e. hourly) whereas satellite measurements are instant snap-shots. Ekman turning of the wind is considered negligible between the sea surface and the measurement height (60 m). Hasager et al. (2004b) have reported a bias of 5° between wind directions given by streaks and meteorological data. Others have found that roll vortices align tens of degrees off the near-surface wind direction (Sikora & Young, 2002).

8.2. Velocity deficit

The classical way of referencing meteorological observations of wind speed is to use upstream measurements of the free stream velocity. In contrast to our expectations, our results show marked differences in the average velocity deficit (VD) for onshore and offshore winds (Fig. 8c). This is a consequence of flow acceleration (speed-up) for offshore and flow deceleration (slow-down) for onshore winds. For onshore flow, the wake effect is combined with decelerated flow causing a high VD (13%) and no apparent wind speed recovery over the downstream distance studied. For offshore flow, speed-up effects outweigh VD such that the maximum VD (4%) decreases to negative values with distance downstream. A severe limitation of the classical reference method is that it does not take spatial changes of the free stream velocity into account.

Our study shows that it is possible to correct for speed-up and slow-down effects if the free stream flow conditions are comparable in two parallel transects. The reference velocity deficit (VD_{ref}) shows similar variations for onshore and offshore winds (Fig. 9c). In both cases, VD_{ref} peaks near the downstream wind farm boundary at 8–9%. A second, remarkable peak is observed between 10 and 15 km downstream. Only one peak of VD_{ref} is expected downstream of wind farms. However, we have demonstrated in Fig. 9a and b that wakes extend more than 20 km downstream for some of the cases investigated, whereas in other cases, VD_{ref} approaches 2% shortly after the wind farms. Naturally, this leads to some fluctuation in the average VD_{ref} .

Wake meandering or bathymetry could possibly cause the fluctuating VD_{ref} downstream of wind farms. If wake meandering occurs, linear transects of boxes may fail to match the wakes. However, due to the width of boxes (3.2 km) and careful selection of the appropriate wind direction, chances are good that wakes are captured. A total of 10 SAR scenes showing bathymetry effects have been deselected early in the study. It is therefore unlikely, that bathymetry has a major influence on the results.

The magnitude and extent of wind wakes is determined by several factors. Those we have addressed include the ambient wind speed, the atmospheric stability, and the number of turbines in operation. Since wind wakes result from a combination of these factors, it is difficult to point out any general measures of wake magnitude and extent for a given free stream velocity; at least from the observations available here. Frandsen and Hauge Madsen (2003) have measured strong wake deficits between 5 and 13 $m s^{-1}$ with a maximum around 8–10 $m s^{-1}$ for the hub-height 31 m. Projecting the wind speeds down to 10 m would lead to lower values consistent with our finding of velocity deficits above 10% for wind speeds of 4.8–6.9 $m s^{-1}$ only. Within the same interval of wind speed, much lower deficits are also observed, indicating the complexity in wake behaviour.

Our results show a maximum average VD_{ref} of 8% for unstable and 9% near-neutral atmospheric stability (Fig. 10). The wind speed recovers to match free stream conditions within $\pm 2\%$ at only 4 km downstream for unstable cases. For near-neutral stability, VD_{ref} remains above 2% over the downstream distance investigated (21 km). The calculated Ri_B values apply to a height of 55 m, which is relatively near the turbine hub-height where wind wakes originate. One could argue that estimates of atmospheric stability near the sea surface, where SAR measurements are obtained, are more suitable in our case. Such estimates require simultaneous measurements of air temperature and sea surface temperature; the latter is typically obtained from optical remote sensors. It is beyond the scope of the present study to analyze thoroughly the atmospheric stability in near shore areas, although the issue is relevant in terms of wind retrievals from SAR.

More than one third of the wind turbines at Horns Rev are operating during satellite passes, except on 19 August

2003. Wake effects are thus expected and observed. It is surprising that VD_{ref} is $\sim 11\%$ on 19 August 2003 with only six turbines in operation. One explanation may be that additional turbines were operating on the day, but failed to report data on their production. A relation between the number of turbines in operation and VD_{ref} is difficult to establish. Several studies (e.g. Crespo et al., 1999; Frandsen et al., 2004) have shown steep declines of wind speed between the first and second wind turbine in a row, whereas additional turbines are exposed to flow conditions fairly similar to the second turbine. If the same concept is applicable to turbines configured in large arrays, wake effects measured downstream of a wind farm are not expected to change much, once a certain fraction of turbines are running. Obviously, the spatial distribution of running turbines within the array is important, especially at times when a relatively low fraction of turbines are in operation.

8.3. Accuracy of velocity deficits

The maximum wind speed reduction of 8–9% found downstream of wind farms corresponds to an absolute reduction of $0.5\text{--}1.5\text{ m s}^{-1}$. The reduction may seem small compared to the $\pm 1.3\text{ m s}^{-1}$ absolute accuracy of SAR wind speeds found through comparison to in situ measurements (Hasager et al., 2004b). However, the accuracy of relative wind speeds is much better. Common errors in SAR measurements (i.e. calibration errors, speckle noise and errors on wind direction) are limited as measured wind speeds are related to the free stream velocity. Since we are concerned with a small part of each SAR image where wind farms are located, errors that depend on ground range distance are negligible.

8.4. Velocity deficits vs. wake model results

State-of-the-art wake models suggest maximum velocity deficits of 12–16% at hub-height with the ambient wind speed 10 m s^{-1} (Barthelmie & Pryor, in press). The spatial extent of wind wakes predicted by the same models is 5–14 km. Maximum SAR-derived velocity deficits (8–9%) are valid at 10 m, but corresponding deficits at hub-height (70 m) are presumably higher. The consistency between modeled and SAR-derived velocity deficits is therefore good. For wind speeds in the range $4\text{--}12\text{ m s}^{-1}$, we have found that wakes extend 5–20 km downstream of offshore wind farms. The wake phenomena can be visually detected on selected SAR images over more than 20 km. This indicates that the spatial extent of wind wakes may be under-estimated by wake models in some situations.

8.5. Turbulence intensity

Our results suggests that SAR images provide realistic turbulence intensities for offshore conditions. Since we are

aiming to quantify turbulence added by wind turbines, *relative* estimates of turbulence intensity (i.e. conditions upstream versus downstream of wind farms) are satisfactory for the study. Image statistics obtained within four boxes (Fig. 6) have allowed a comparison of turbulence intensity upstream and downstream of the wind farms at Horns Rev and Nysted. The change in ambient turbulence intensity due to changing distance from the shoreline has been estimated. Ultimately, turbulence intensity added by the turbines has been isolated. The turbulence intensities found in the non-obstructed flow are not always comparable when boxes are displaced 8 km apart. Variations in ambient turbulence intensity may result from a different fetch with offshore winds or could be an effect of atmospheric features varying in space (e.g. roll vortices).

Added turbulence intensity is found downstream of wind farms for 7 of 19 cases. Another 7 cases show higher turbulence intensity upstream than downstream of the wind farms. For offshore winds, this may be due to residual land influence on the ambient flow. In contrast to the mean wind speed, turbulence intensity generally decreases with distance offshore (Barthelmie & Pryor, in press). Another possible explanation is that turbulence generated by wind turbines has no impact at surface level. Measurements by Frandsen and Christensen (1994) indicate that, although a significant increase of standard deviation of wind speed is observed at hub-height, the standard deviation remains unchanged near the ground or, for high wind speeds, it decreases.

9. Conclusion

Satellite SAR data have been used to quantify wake velocity deficits near two large offshore wind farms. Using a parallel transect for normalization of wind speeds in the wake areas is preferred to using an upstream, fixed point of reference. The former reference method eliminates land effects e.g. speed-up for offshore winds. A significant reduction (8–9%) of the mean wind speed is observed in SAR wind speed maps as the wind flow passes through large arrays of wind turbines. Wind speed recovers to within 2% of the free stream velocity over a downstream distance of 5 km for unstable and 20 km for near-neutral conditions. The magnitude and extent of measured wind wakes are consistent with results from wake models and in situ measurements. Turbulence intensity upstream and downstream of wind farms have been compared based on the SAR wind speed maps. Results are ambiguous, possibly due to large differences between turbulence intensity at hub-height and near the sea surface where SAR measurements are obtained. We have shown that realistic measures of turbulence intensity can be obtained from satellite SAR. Further, variations in space can be identified, that may be related to wake generated turbulence. The application of high resolution wind speed measurements from satellite SAR is new in wind energy. The spatial information gained

from SAR data is useful for environmental impact studies of large offshore wind farms and in the planning of new wind farm projects.

Acknowledgements

Funding for our study is provided through the SAR-WAKE project (26-02-0312), Danish Technical Research Council (STVF). The satellite images are granted from the European Space Agency in Cat. 1 project EO-1356. Elsam Engineering A/S is thanked for meteorological data and DHI Water and Environment for bathymetry data. Dr. Frank Monaldo and Dr. Donald Thompson are kindly thanked for comments and suggestions as well as for hospitality during our visits at The Johns Hopkins University, Applied Physics Laboratory in Maryland, USA. At Risø National Laboratory, Dr. Jake Badger is thanked for programming assistance and Dr. Rebecca Barthelmie for discussions about wind wakes. Comments from three anonymous reviewers have improved the quality of our paper significantly.

References

- Attema, E., Desnos, Y. -L., & Duchossois, G. (2000). Synthetic aperture radar in Europe: ERS, Envisat and beyond. *Johns Hopkins APL Technical Digest*, 21, 155–161.
- Barthelmie, R. J. (1999). The effects of atmospheric stability on coastal wind climates. *Meteorological Applications*, 6, 39–48.
- Barthelmie, R. J., & Pryor, S. (in press). Challenges in predicting power output from offshore wind farms. *Journal of Energy Engineering on Sustainable Energy Systems*.
- Barthelmie, R. J., Folkerts, L., Ormel, F. T., Sanderhoff, P., Eecen, P. J., Stobbe, O., et al. (2003). Offshore wind turbine wakes measured by sodar. *Journal of Atmospheric and Oceanic Technology*, 20, 466–477.
- Barthelmie, R., Giebel, G., Jørgensen, B. H., Badger, J., Pryor, S. C., & Hasager, C. B. (2004a). Comparison of corrections to site wind speeds in the offshore environment: Value for short-term forecasting. *Scientific proceedings. 2004 European Wind Energy Conference and Exhibition, London (GB)*, 22–25 Nov. 2004. London: European Wind Energy Association.
- Barthelmie, R., Larsen, G., Bergström, H., Magnusson, M., Schlez, W., Rados, K., et al. (2004b). ENDOW (Efficient Development of Offshore Windfarms): Modelling wake and boundary layer interactions. *Wind Engineering*, 7, 225–245.
- Barthelmie, R. J., Pryor, S. C., Frandsen, S., & Larsen, S. E. (2004c). Analytical modelling of large wind farm clusters. *Proceedings special topic conference: The science of making torque from Wind, Delft (NL)* (pp. 292–303).
- Betz, A. (1920). Der Maximum der theoretisch möglichen Ausnutzung des Windes durch Windmotoren. *Zeitschrift für das gesamte Turbinenwesen*, 26, 307–309.
- Christiansen, M. B. (2004). Wind energy studies offshore using satellite remote sensing. *19th World Energy Congress Sydney (AU)*, 5–9 Sep 2004.
- Chunchuzov, I., Vachon, P. W., & Li, X. (2000). Analysis and modeling of atmospheric gravity waves observed in RADARSAT SAR images. *Remote Sensing of Environment*, 74, 343–361.
- Clemente-Colón, P., & Yan, X. H. (2000). Low-backscatter ocean features in synthetic aperture radar imagery. *Johns Hopkins APL Technical Digest*, 21, 116–121.
- Crespo, A., Hernández, J., & Frandsen, S. (1999). Survey of modelling methods for wind turbine wakes and wind farms. *Wind Energy*, 2, 1–24.
- Du, Y., Vachon, P. W., & Wolfe, J. (2002). Wind direction estimation from SAR images of the ocean using wavelet analysis. *Canadian Journal of Remote Sensing*, 28, 498–509.
- EWEA. (2004). *Security of energy supply: Offshore wind can be the answer to Europe's energy crunch*. News release at. www.ewea.org
- Fichaux, N., & Rachin, T. (2002). Combined extraction of high spatial resolution wind speed and direction from SAR images: A new approach using wavelet transform. *Canadian Journal of Remote Sensing*, 28, 510–516.
- Frandsen, S., Barthelmie, R., Pryor, S., Rathmann, O., Larsen, S., Højstrup, J., et al. (2004). Analytical modelling of wind speed deficit in large offshore wind farms. *Scientific proceedings. 2004 European Wind Energy Conference and Exhibition London (GB)*, 22–25 Nov 2004. London: European Wind Energy Association.
- Frandsen, S., Chacón, L., Crespo, A., Enevoldsen, P., Gómez-Elvira, R., Hernández, et al. (1996). *Measurements on and modelling of offshore wind farms*. Risø-R-903(EN), Risø National Laboratory (DK).
- Frandsen, S., & Christensen, J. C. (1994). Vindeby Offshore Windfarm — fatigue measurements. *EWEC '94 Conference, Thessaloniki, Greece, 10–14 Oct 1994*, Unpublished.
- Frandsen, S., & Hauge Madsen, P. (2003). Spatially average of turbulence intensity inside large wind turbine arrays. *Offshore wind energy in Mediterranean and other European seas. Resources, technology, applications. OWEMES 2003. European seminar Naples (IT)*, 10–12 Apr 2003. Naples: Univ. of Naples.
- Frandsen, S., & Thomsen, K. (1997). Change in fatigue and extreme loading when moving wind farms offshore. *Wind Engineering*, 21, 197–214.
- Garratt, J. R. (1990). The internal boundary layer—a review. *Boundary–Layer Meteorology*, 50, 171–203.
- Gerling, T. W. (1986). Structure of the surface wind field from the Seasat SAR. *Journal of Geophysical Research*, 91, 2308–2320.
- Hasager, C. B., Barthelmie, R. J., Christiansen, M. B., Nielsen, M., & Pryor, S. C. (2004a). Quantifying offshore wind resources from satellite wind maps: Study area the North Sea. *Scientific proceedings. 2004 European Wind Energy Conference and Exhibition London (GB)*, 22–25 Nov 2004. London: European Wind Energy Association.
- Hasager, C. B., Dellwik, E., Nielsen, M., & Furevik, B. (2004b). Validation of ERS-2 SAR offshore wind-speed maps in the North Sea. *International Journal of Remote Sensing*, 25, 3817–3841.
- Hasager, C. B., Nielsen, M., Astrup, P., Barthelmie, R., Dellwik, E., Jensen, N. O., et al. (in press). Offshore wind resource estimation from satellite SAR wind field maps. *Wind Energy*.
- Horstmann, J., & Koch, W. (2003). High resolution ocean surface wind fields retrieved from spaceborne synthetic aperture radars operating in C-band. *Proceedings of the Second Workshop on Coastal and Marine Applications of SAR, Svalbard (N)*.
- Horstmann, J., Lehner, S., Koch, W., & Tonboe, R. (2000). Computation of wind vectors over the ocean using spaceborne synthetic aperture radar. *Johns Hopkins APL Technical Digest*, 21, 100–107.
- IEA. (2004). *IEA Wind Energy Annual Report 2003. International Energy Agency Executive Committee for the Implementing Agreement for Co-operation in the Research and Development of Wind Turbine Systems*. http://www.ieawind.org/annual_reports.html
- Keith, D. W., DeCarolus, J. F., Denkenberger, D. C., Lenschow, D. H., Malyshev, S. L., Pacala, S., et al. (2004). The influence of large-scale wind power on global climate. *Proceedings of the National Academy of Sciences of the United States of America*, 101, 16115–16120.
- Koch, W. (2004). Directional analysis of SAR images aiming at wind direction. *IEEE Transactions on Geoscience and Remote Sensing*, 42, 702–710.
- Lange, B., Larsen, S., Højstrup, J., & Barthelmie, R. J. (2004). The influence of thermal effects on the wind speed profile of the coastal marine boundary layer. *Boundary–Layer Meteorology*, 112, 587–617.

- Lehner, S., Horstmann, J., Koch, W., & Rosentahl, W. (1998). Mesoscale wind measurements using recalibrated ERS SAR images. *Journal of Geophysical Research*, 103, 7847–7856.
- Lewis, A. J., & Henderson, F. M. (1998). Radar fundamentals: The geoscience perspective. In F. M. Henderson, & A. J. Lewis (Eds.), *Principles and applications of imaging radar: Manual of remote sensing*, 3rd edition, vol. 2 (pp. 131–176). New York: Wiley.
- Li, X., Clemente-Colón, P., Pichel, W. G., & Vachon, P. W. (2000). Atmospheric vortex streets on a RADARSAT SAR image. *Geophysical Research Letters*, 27, 1655–1658.
- Monaldo, F. (2000). The Alaska SAR demonstration and near-real-time synthetic aperture radar winds. *Johns Hopkins APL Technical Digest*, 21, 75–79.
- Monaldo, F., & Kerbaol, V. (2003). The SAR measurement of ocean winds: An overview for the 2nd workshop on coastal and marine applications of SAR. *Proceedings of the Second Workshop on Coastal and Marine Applications of SAR, Svalbard (N)*.
- Monaldo, F. M., Thompson, D. R., Beal, R. C., Pichel, W. G., & Clemente-Colón, P. (2001). Comparison of SAR-derived wind speed with model predictions and ocean buoy measurements. *IEEE Transactions on Geoscience and Remote Sensing*, 39, 2587–2600.
- Monaldo, F. M., Thompson, D. R., Pichel, W. G., & Clemente-Colón, P. (2004). A systematic comparison of QuickSCAT and SAR ocean surface wind speeds. *IEEE Transactions on Geoscience and Remote Sensing*, 42, 283–291.
- Mourad, P. D., Thompson, D. R., & Vandemark, D. C. (2000). Extracting fine-scale wind fields from synthetic aperture radar images of the ocean surface. *Johns Hopkins APL Technical Digest*, 21, 108–116.
- Nielsen, M., Astrup, P., Hasager, C. B., Barthelmie, R. J., & Pryor, S. C. (2004). Satellite information for wind energy applications. *Risø-R-1479(EN)* (pp. 1–57). Roskilde, Denmark: Risø National Laboratory.
- Petersen, E. L., Mortensen, N. G., Landberg, L., Højstrup, J., & Frank, H.P. (1998). Wind power meteorology: Part I. Climate and turbulence. *Wind Energy*, 1, 2–22.
- Roy, S. B., Pacala, S. W., & Walko, R. L. (2004). Can large wind farms affect local meteorology? *Journal of Geophysical Research*, 109, D19101.
- Sikora, T. D., & Young, G. S. (2002). Wind-direction dependence of quasi-2D SAR signature. *Proceedings International Geoscience and Remote Sensing Symposium, Toronto (CA)* (pp. 1887–1889).
- Stoffelen, A., & Anderson, D. (1993). Wind retrieval and ERS-1 scatterometer radar backscatter measurements. *Advances in Space Research*, 13, 53–60.
- Stoffelen, A., & Anderson, D. (1997a). Scatterometer data interpretation: Measurement space and inversion. *Journal of Atmospheric and Oceanic Technology*, 14, 1298–1313.
- Stoffelen, A., & Anderson, D. (1997b). Scatterometer data interpretation: Estimation and validation of the transfer function CMOD4. *Journal of Geophysical Research*, 102, 5767–5780.
- Ulaby, F. T., Moore, R. K., & Fung, A. K. (1982). *Microwave remote sensing, active and passive* (pp. 562–745). Reading, Massachusetts: Addison-Wesley.
- Vachon, P. W., & Dobson, F. W. (1996). Validation of wind vector retrieval from ERS-1 SAR images over the ocean. *Global Atmosphere and Ocean System*, 5, 177–187.
- WEC. (2000). *Energy for tomorrow's world—acting now!* London, UK: WEC http://www.worldenergy.org/wec-geis/publications/reports/etwan/exec_summary/exec_summary.asp
- WEC. (2001). *Survey of energy resources*. London, UK: WEC <http://www.worldenergy.org/wec-geis/publications/reports/ser/overview.asp>
- WEC. (2003). *WEC statement 2003—renewable energy targets*. London, UK: WEC <http://www.worldenergy.org/wec-geis/publications/statements/stat2003.asp>
- Young, G., & Winstead, N. (2004). Meteorological phenomena in high resolution SAR wind imagery. In B. Beal, G. Young, F. Monaldo, D. Thompson, N. Winstead, & C. Scott (Eds.), *High resolution wind monitoring with wide swath SAR: A user's guide* (pp. 13–34). Online at http://fermi.jhuapl.edu/sar/stormwatch/user_guide